

SKY VARIABILITY IN THE y BAND AT THE LSST SITE

F. WILLIAM HIGH, CHRISTOPHER W. STUBBS & BRIAN STALDER

Department of Physics
and
Harvard-Smithsonian Center for Astrophysics
Harvard University, Cambridge, MA 02138 USA

DAVID KIRK GILMORE

Kavli Institute for Particle Astrophysics and Cosmology
Stanford Linear Accelerator Center
Sand Hill Road, Palo Alto, CA 94025 USA

JOHN L. TONRY

Institute for Astronomy
University of Hawaii
2680 Woodlawn Drive, Honolulu, HI 96822 USA
Draft version November 3, 2018

ABSTRACT

We have measured spatial and temporal variability in the y band sky brightness over the course of four nights above Cerro Tololo near Cerro Pachon, Chile, the planned site for the Large Synoptic Survey Telescope (LSST). Our wide-angle camera lens provided a 41° field of view and a $145''$ pixel scale. We minimized potential system throughput differences by deploying a deep depletion CCD and a filter that matches the proposed LSST y_3 band (970 to 1030 nm). Images of the sky exhibited coherent wave structure, attributable to atmospheric gravity waves at 90 km altitude, creating 3% to 4% rms spatial sky flux variability on scales of about 2 degrees and larger. Over the course of a full night the y_3 band additionally showed highly coherent temporal variability of up to a factor of 2 in flux. We estimate the mean absolute sky level to be approximately $y_3 = 17.8$ mag(Vega), or $y_3 = 18.3$ mag(AB). While our observations were made through a y_3 filter, the relative sky brightness variability should hold for all proposed y bands, whereas the absolute levels should more strongly depend on spectral response. The spatial variability presents a challenge to wide-field cameras that require illumination correction strategies that make use of stacked sky flats. The temporal variability may warrant an adaptive y band imaging strategy for LSST, to take advantage of times when the sky is darkest.

Subject headings: atmospheric effects, instrumentation: photometers, techniques: photometric, spectroscopic

1. INTRODUCTION

The Large Synoptic Survey Telescope (LSST) is a proposed wide-field camera that is currently in the design and development phase (LSST Science Collaborations: Paul A. Abell et al. 2009, hereafter LSST09). The project has designated the telescope's site to be Cerro Pachon, Chile, on the same ridge that hosts the Gemini South and SOAR telescopes. The LSST will survey the sky in the Sloan Digital Sky Survey's *ugriz* passbands, plus an additional near infrared band, y , at wavelengths ~ 990 nm, only recently made possible by deep depletion CCD technology that enhances quantum efficiency (QE) at the reddest wavelengths (O'Connor et al. 2006). The Pan-STARRS (Kaiser et al. 2002) survey also uses the y band.

The designation of “ y ” may present confusion. Infrared astronomers use a band Y , typically with a central wavelength near $1.03\mu\text{m}$ (Hillenbrand et al. 2002; Hewett et al. 2006). Their use of infrared detectors, with a flatter response curve near a micron, yields a passband

with significantly different shape than the CCD-based y . Our filter also bears no relation to the optical y filter of the Stromgren passbands, which is centered on 550 nm. This degeneracy in terminology is most unfortunate, but seems likely to persist.

The sky brightness in the y band has not been well characterized for astronomical CCD applications. Past work describing sky brightness at observatories typically cite values for the *UBVRI* bands, but not y (Patat 2003; Krisciunas et al. 2007; Sanchez et al. 2007). The reddest band in the SDSS survey is z , whose red edge is determined by the rapidly falling QE of the SDSS detectors, which have very little sensitivity in the y band region. The UKIRT survey presented sky measurements for the Y band (Warren et al. 2007), but as explained before, the total transmission curve is significantly different than that using a deep depletion CCD.

Our aim has been to provide the first dedicated CCD measurements, at the proposed LSST site, of the y band sky background and its variability over the course of a night. While the exact character of the new y band to be used for LSST is under active consideration, we used

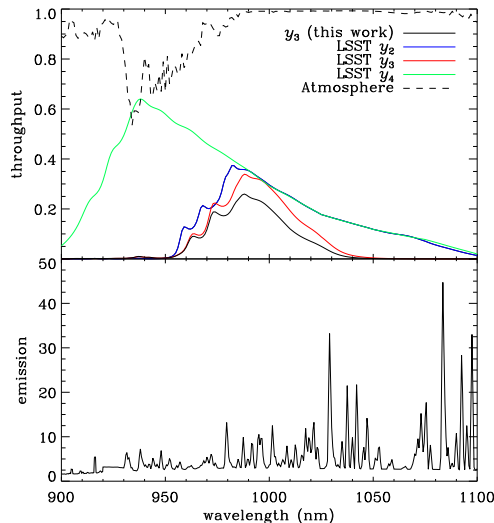


FIG. 1.— The LSST y band and its variants (top), and the sky emission spectrum (bottom). The top panel shows the expected transmission spectrum for proposed y band variants (LSST Science Collaborations: Paul A. Abell et al. 2009) including predicted optics and detector response, as well as the relative transmission that we measure for our apparatus (black solid line). Our effective filter curve closely resembles the planned y_3 band. All spectra exclude atmospheric absorption and scattering, which we plot separately as a dashed line. The bottom panel shows a typical sky spectrum in photons $\text{s}^{-1} \text{m}^{-2} \text{nm}^{-1} \text{arcsec}^{-2}$, dominated by Meinel band OH emission lines (taken from Puxley et al. 2001).

a filter candidate called y_3 (LSST09). We expect our qualitative findings to hold for any y band variant under active consideration because the sky background in all cases arises overwhelmingly from narrow OH emission lines. Figure 1 shows potential y band transmission curves with detector quantum efficiency (QE) and atmospheric response for both LSST and our apparatus, along with the anticipated sky emission spectrum.

In §2 we briefly describe the known nature of sky emission within the y passband, covering past aeronomic (§2.1) and astronomical (§2.2) measurements. In §3 we describe the dedicated instrument we assembled for these measurements. Section 4 discusses the observations, and the data reduction is outlined in §5. Section 6 presents results on spatial (§6.1) and temporal (§6.2) variability, and an absolute calibration (§6.3), and we conclude with §7.

2. THE NATURE OF Y BAND SKY BACKGROUND

The background sky in the y passband is dominated by Meinel band emission due to hydroxyl (Meinel 1950a,b), in a physical process that has long been observed (eg Wiens et al. 1997; Nakamura et al. 1999) and modeled (Rousselot et al. 2000; Cosby et al. 2006; Cosby & Slanger 2007) by atmospheric scientists (for a useful overview, see Marsh et al. 2006). Hydroxyl is well stratified in the mesopause at 90 km in a 10 km thick layer (Baker & Stair 1988; Melo et al. 2000). Above the ozone layer in the stratosphere, daytime UV light from the sun dissociates O_2 to make $\text{O} + \text{O}$, which react with other O_2 to produce O_3 . UV light also dissociates O_3 , completing the oxygen-ozone cycle. O_3 additionally reacts with H to produce O_2 and excited OH, which then emits photons to produce the airglow within the y band.

As distinct from Rayleigh scattering, Meinel emission is known to vary significantly over a number of spatial and temporal scales (eg Marsh et al. 2006). The airglow varies with the tides, and is linked to the seasons and the solar cycle. Traveling and standing atmospheric gravity waves, which are coherent density perturbations analogous to ocean waves, are regularly observed by aeronomers (eg Taylor & Hill 1991; Garcia et al. 1997; Nakamura et al. 1999; Li et al. 2005), and give rise to a variable background over a single, wide-field y band CCD image.

2.1. Aeronomic Measurements

Aeronomers, like astronomers, have made extensive use of CCDs since their invention, but also have not explored the y passband region with them in depth because the development of deep depletion is recent. CCDs have been used to measure sky emission lines in isolation with Fabry-Perot interferometers, for the purpose of monitoring atmospheric gravity waves and variability in species temperature and emission rate (eg, the Spectral Airglow Temperature Imager, SATI, Wiens et al. 1997). They have also been used to image gravity waves directly with narrow and broad filters (eg Taylor & Hill 1991; Garcia et al. 1997; Li et al. 2005). These applications have been most often used in concert with radar, lidar, balloons, rocketry, and space-based experiments to achieve fully three-dimensional dynamical information of O_2 and OH atmospheric layers. None of these observations ventured far into the red of today’s deep depletion CCDs, nor did the analyses achieve calibrated photometry. Existing aeronomic data are therefore of limited use to LSST, as LSST requires prior knowledge not only of the variability but also of the expected absolute background level in the y channel. Our instrument and data reduction techniques aim to provide all needed information at once.

2.2. Previous Astronomical Measurements

Previous astronomical work is also insufficient, as the y band sky has not been directly characterized. Extrapolating to the y band using other astronomical filters is problematic because of the highly structured nature of the Meinel band emission (Figure 1, bottom panel). Small changes in the filter’s red edge may suddenly alter the background level. For example, the recent UKIRT survey (Warren et al. 2007) does include a Y band, but using an infrared detector and filter whose total response function do not match that expected for LSST. Warren et al. (2007) in fact showed that their Z band sky brightness from the UKIRT observations on Mauna Kea was $0.4 \text{ mag arcsec}^{-2}$ brighter than that obtained by SDSS in their z band, at Apache Point, New Mexico. Besides differences in effective filtering, the discrepancy may be explained by differences in atmospheric conditions in time and in space given the great geographical separation. We therefore must assume that the UKIRT median sky brightness of $Y = 17.4 \text{ mag arcsec}^{-2}$ (Vega) cannot be applied to LSST.

Our effective filter function closely matches LSST’s y_3 band and thus minimizes potential errors due to differences in relative spectral response; we additionally address the geographical problem by observing at Cerro

Tololo, a mountain ridge 10 km northwest of LSST’s planned site, Cerro Pachon. Krisciunas et al. (2007) presented a historical overview of sky brightness observations from Cerro Tololo, for the period 1992–2007. They claimed that there was no discernable difference in sky brightness between that site and Cerro Pachon. This leads us to conclude that our y band sky brightness measurements from Tololo should be applicable to the LSST site on Pachon.

We conclude that previous work within aeronomy and astronomy is not sufficient for characterizing the y band sky background for LSST, and that the precise nature of the chosen y filter affects the observed background due to the multitude of strong OH lines at $\sim 1 \mu\text{m}$ and redder. The dependence of the apparent NIR sky brightness on the filter and detector combination, and the potential for variation between observatory sites, motivates the measurements described here.

3. APPARATUS

We used a Pixis system (detector, readout electronics, dewar and shutter) from Princeton Instruments, equipped with a type 1024BR CCD. This detector, made by EEV with their designation 47-10, was a back-illuminated deep depletion sensor that exhibits enhanced sensitivity at wavelengths near 900 nm due to the thicker region of silicon from which photocharge is harvested. The sensor was an array of 1040×1027 pixels, each of which was $13.0 \mu\text{m}$ on a side. The Pixis camera was equipped with a thermoelectric cooler that maintained the detector at a temperature of -20 C . Dark current was negligible compared to the flux seen from the sky. We measured the camera’s gain to be $3.8 e^- \text{ ADU}^{-1}$.

Princeton Instruments designed the 1024BR CCD to suppress fringing that would otherwise arise from night sky line emission. We observed no significant fixed fringing patterns in any of the images we obtained, and did not have to apply any fringe-frame corrections to the data. We therefore judge any systematics in the photometry due to fringing to be subdominant for the purposes of the results presented here.

The Pixis camera was controlled from a laptop computer that ran the Linux operating system. We used custom software to control the exposure times and imaging sequence of the instrument. All images were stored as 16 bit FITS files.

We attached a 17–55 mm variable focal length $f/2.8$ Canon EFS lens to the Pixis dewar, using a C-mount adapter made by Birger Engineering. The system was operated at $f/2.8$. The y filter we used was an interference filter manufactured to the LSST y_2 specification by Barr Associates, in a 2 in \times 2 in format. We attached the filter to the front of the lens using a modified professional photography filter holder that mated to the 75 mm front threads of the Canon lens. The lens’s focal length was adjusted so as to provide a plate scale of $145'' \text{ pixel}^{-1}$, and a square field of view of 41° . Although we make use of a y_2 filter, the resultant system throughput more closely matches the LSST y_3 response curve due to the difference in our detector QE and antireflection coatings on the optics from the predicted LSST system.

The camera, lens and filter combination was mounted on a stationary tripod. This arrangement did not provide pointing information in the image headers, but as

described below we were later able to determine astrometry using the positions of cataloged sources.

Our optical configuration was not identical to that of LSST. The LSST filters will be placed in an $f/1.23$ converging beam. Light from a point source therefore passes through the LSST filter in a (hollow) cone with an opening half-angle between 14.2° and 23.6° . Obscuration from the secondary blocks rays at angles less than 14.2° . The transmission curve through the interference filter depends on the angle of incidence. Rays that traverse the filter at angles θ other than normal incidence produce a blue shifted transmission function, shifted to the blue by roughly

$$\delta\lambda = \lambda \left[\sqrt{1 - n^{-1} \sin^2(\theta)} - 1 \right] \quad (1)$$

where n is the effective index of refraction of the filter dielectric. The effective LSST passband is the appropriately weighted integral of these angle-dependent transmission functions.

For our observations we placed the filter in front of the lens, so rays from any point source pass through the filter as parallel rays. The center of our field is observed through the filter at normal incidence. The edges of our field are observed through the filter at an incidence angle of 20° . While we can’t replicate the *distribution* of rays that will pass through the LSST filters, by judiciously choosing the region in our field where we measure the sky brightness, we can try to match the median LSST ray that traverses the filter at an angle of 18.9° (LSST09). We therefore expect, even for a perfect match between our interference filter and that of LSST, slight differences in the effective passbands. See Figure 1 for a comparison of passbands.

4. OBSERVATIONS

We obtained images over four nights, UT 2007 Sep 13, 14, 18, and 19. On the 13th we acquired data on the second half of the night, and pointed the camera on the local meridian and low to the horizon at a zenith angle of about 60° . For the remaining nights we aimed the camera on the local meridian toward the equatorial, at approximately 30° north.

The moon was 6% illuminated on the first two nights and set at $01^{\text{h}}43^{\text{m}}$ UT. The moon was 44% illuminated on the last two nights and rose at $05^{\text{h}}30^{\text{m}}$ UT. For the all observations, the moon was not a complicating factor. We estimate that the conditions on the first two nights were photometric, whereas high clouds began to form on the second half of the 18th and all of the 19th. Table 1 summarizes the observations.

On each night we elected to take all images at a fixed azimuth and elevation in order to simplify our analysis of the temporal variation in sky brightness. The nominal pointing changed somewhat from night to night, however, because we disassembled the apparatus each morning. We did not track the camera in R.A. We alternated between sequences of five 20 s (“short”) exposures and ten 300 s (“long”) exposures throughout the night. On the 14th we acquired a total of 55 short exposures and 110 long exposures. The short frames had only slight trailing of stars, and were useful for astrometry and photometric normalization using the normal toolkit of astronomical data reduction for point sources. The longer

TABLE 1
SUMMARY OF THE DATA.

| Night ^a | Num exposures | | Conditions ^b |
|--------------------|---------------|------|---------------------------------|
| | 5 min | 20 s | |
| 2007 09 13 | 54 | 31 | Photometric |
| 2007 09 14 | 111 | 58 | Photometric |
| 2007 09 18 | 76 | 40 | First half of night photometric |
| 2007 09 19 | 67 | 35 | Clouds |

^a Local date at start of night.

^b Based on our observations, archived SASCA red-channel animations (see <http://www.ctio.noao.edu/~sasca/sasca.htm>), GOES East 10 micron satellite imagery (see <http://www.ctio.noao.edu/sitetests/GOES/>), CTIO DIMM and flux monitor data, and Blanco Cosmology Survey observers' logs.

images offered better signal to noise for the sky brightness, but stars trailed significantly in the EW direction.

5. DATA REDUCTION

We used the utilities in IRAF to do a line-by-line bias subtraction of each of the images, using the overscan. The 300 s exposures were combined into a normalized sky flat, by taking a flux-scaled median of the frames. This normalized sky flat was then used to flat-field each of the images. The normalized sky flat had a fractional response suppression of about 20% from the center to the corners of the field, presumably due to vignetting and perhaps plate scale variation from the lens. This variation in flux sets an upper bound for potential systematic errors in sky brightness due to passband dependence on the angle of incidence, at 0.2 mag. We take this as an extreme upper limit, since we do expect \cos^n factors to roll off the response at the edges of the field. Because we are measuring sky brightness, the stacked sky flat is indeed appropriate for correcting the pixel-to-pixel variations on the scale of a PSF. Our $41^\circ \times 41^\circ$ field of view rendered twilight flat-fielding impossible due to sky gradients over such a large field and to the short window of time over which useful sky levels per pixel could be acquired, and we had no system in place for obtaining the equivalent of dome-flats. As noted in §3, the 1024BR CCD was specifically designed to suppress fringing, and indeed we observed no fringe patterns in any of our data and therefore made no fringe-frame corrections. Figures 2 and 3 show typical long exposures, after flat-fielding and bias subtraction.

6. RESULTS

We first explored relative measurements of the sky background, because we expect relative errors to be significantly smaller than the overall uncertainty from absolute zeropoint calibration. We then estimated the overall zeropoint in the Vega and AB magnitude systems.

6.1. Spatial Variability

The gravity waves we observed in the vast majority of our images are easily seen in Figure 2 and 3. These structures were not due to flatfielding errors. This can be deduced from the two example images themselves, which were taken from the same night and had the same flatfield correction applied to them. Roughly speaking, the locations of large-scale brightness minima in Figure 2 correspond to maxima in Figure 3. Indeed, these waves

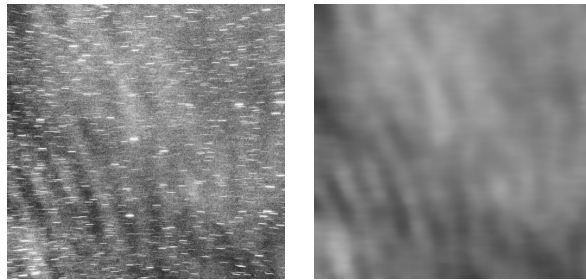


FIG. 2.— A flat-fielded 300 s exposure in y_3 , taken at fixed altitude and azimuth (righthand frame has stars removed to emphasize the airglow structure). The star trails subtend about 1.25° in the EW direction; north is up and east is right. This image shows two distinct gravity waves traced by NIR narrowband emission, which gives rise to short term variability in y_3 band sky brightness. The high frequency ripples have wavelength of about 5 deg and propagate at between zero and about a degree per minute. The low frequency ripple's wavelength is roughly the field of view (40 deg) and travels at a degree per minute. Root mean square sky variations in a given frame are up to 4%, while the overall sky level over a full night varies by a factor of 2.

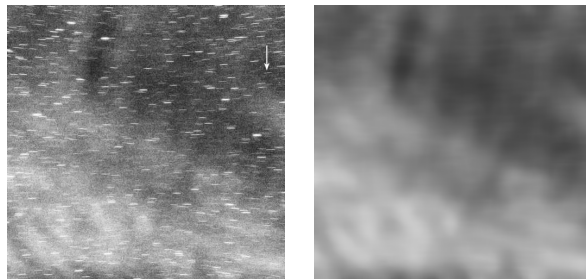


FIG. 3.— Same as Figure 2, but taken later in the night, just as our calibration star ρ Ceti entered the field of view (upper right corner of lefthand frame).

appear and disappear, and move coherently in images from any given night viewed consecutively. Their direction of propagation is perpendicular to their wavefronts.

To quantitatively estimate the effect of the waves on sky brightness at any given time, we computed the mode of the sky brightness values for three regions of the detector, for each of the flatfielded 300 s images. The reference region was the central 500×500 pixel area of the detector. This was used to estimate the zero-level over the large area of sky that we observed. Our “calibrator” region was a smaller, circular aperture of radius 50 pixels near the detector corner that we ultimately used for zeropoint calibration (§ 6.3). The “control” region was another 50 pixel radius aperture near the opposite corner, but at the same angle of incidence with respect to the camera bore-sight. The calibrator and control regions were chose to be smaller than the size of the smallest coherent spatial gravity waves in the images, whereas the reference region was chosen to be much larger.

We calculated the mode of pixel values in each aperture to attain sky counts c in ADU pixel^{-1} . Relative magnitudes between each corner region and the central reference region were calculated as $\Delta\Sigma = 2.5 \log(c_{\text{cal}}/c_{\text{ref}})$, (likewise for $c_{\text{ctrl}}/c_{\text{ref}}$) with units of mag arcsec^{-2} , assuming a common pixel scale between the two apertures. Figure 4 shows these fractional differences over each night.

Observations on the night of the 13th were taken at $\sec(z) = 2$ airmasses at the center of the detector, with the calibrator region at 1.4 airmasses and the control re-

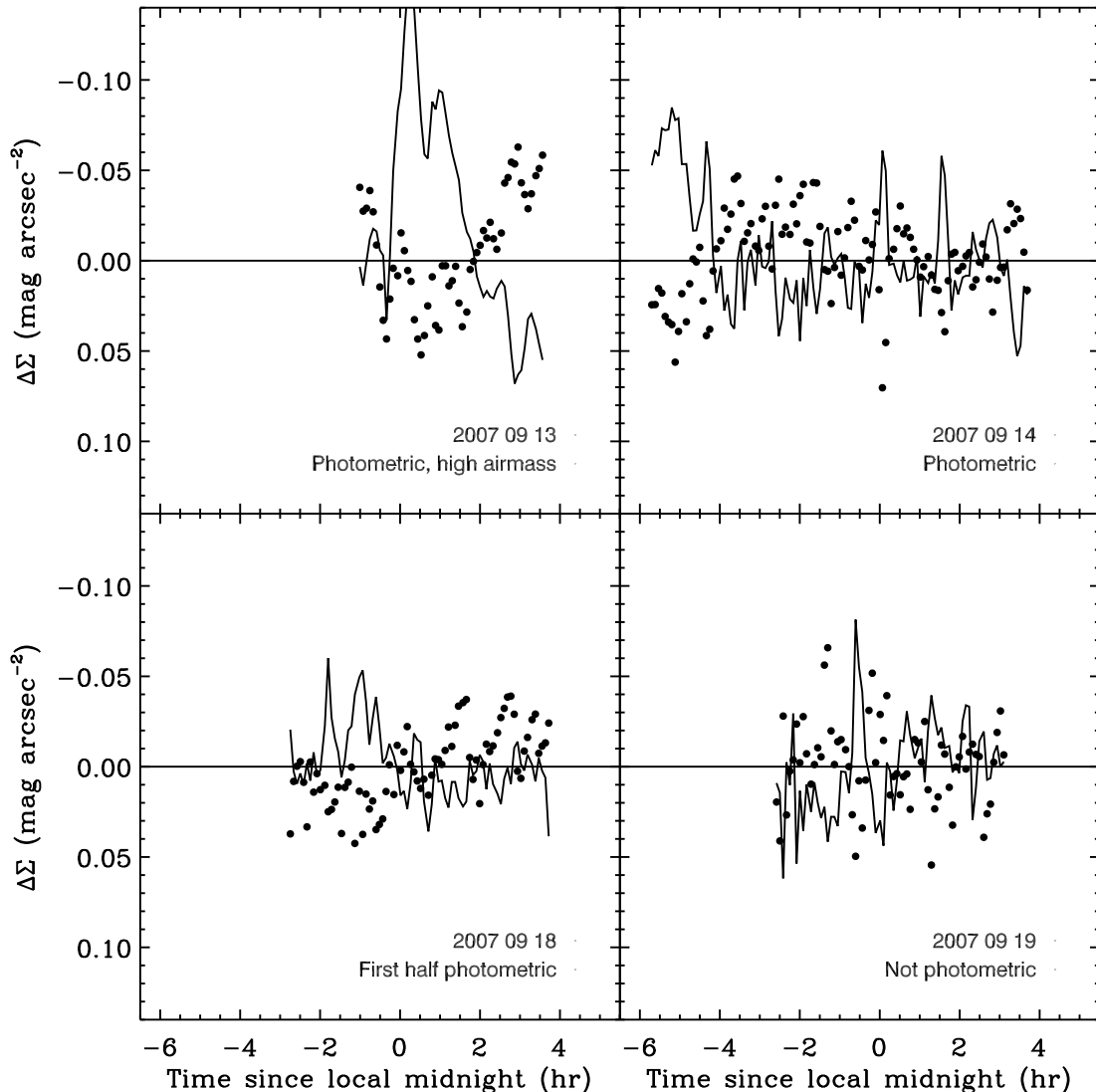


FIG. 4.— Spatial variation in y_3 band sky brightness versus time, showing 2%–5% rms variability in flux. This plot shows the fractional difference in sky brightness between our calibrator region (circular aperture of radius 50 pixels) versus a central reference region of size 500×500 pixels (points), and between a second 50 pixel radius region on the opposite corner of the chip and the reference region (line). The large variation on the 13th is due to the extreme difference in airmass between two corner regions: 5.8 for the northeast corner and 1.3 for the southwest corner. Early on in the night on the 14th, the Galactic plane fell within the NW aperture, again causing larger than typical variation.

gion at approximately 4 airmasses, due to our large field of view. This gave rise to rms spatial sky brightness variations of 3% between the calibrator and the reference region, 6% between the control and the reference region, and 8% between the calibrator and control regions. On the other three nights, the camera pointed at about 1.2 air masses, with the calibrator region at 1.0 air masses and the control region at 1.4 air masses. Ignoring the early part of the 14th, where the Galactic plane fell within the control region, these nights exhibited 2%–3% rms spatial variability with respect to the reference, and 3%–4% rms variability between the calibrator and control regions. We conclude that, on angular scales of the wavelength of the gravity waves, $\gtrsim 2\%$, the spatial variability in the y band is typically 3%–4% rms. Our relative photometric errors are expected to be subdominant to this effect. Under the assumptions that gain, exposure

time, and pixel scale are all constant in any given image, these results are independent of those quantities and of any absolute flux calibration.

6.2. Temporal Variability

The overall temporal sky variability is estimated using a similar approach as in the previous section. The fluxes within the 500×500 pixel reference region are compared to the mean over all 4 nights, and plotted in Figure 5. Here we are comparing 2.5 times the log of sky counts in ADU pixel^{-1} *between* images rather than within them, but because all exposure times, gain values, and pixel regions (and therefore pixel scales) were the same, this is equivalent to measuring relative sky brightness in mag arcsec^{-2} . Again, all that needs to be done to bring this to an absolute scale is to add a zeropoint in mag arcsec^{-2} .

Immediately evident both in the Figure and in the raw

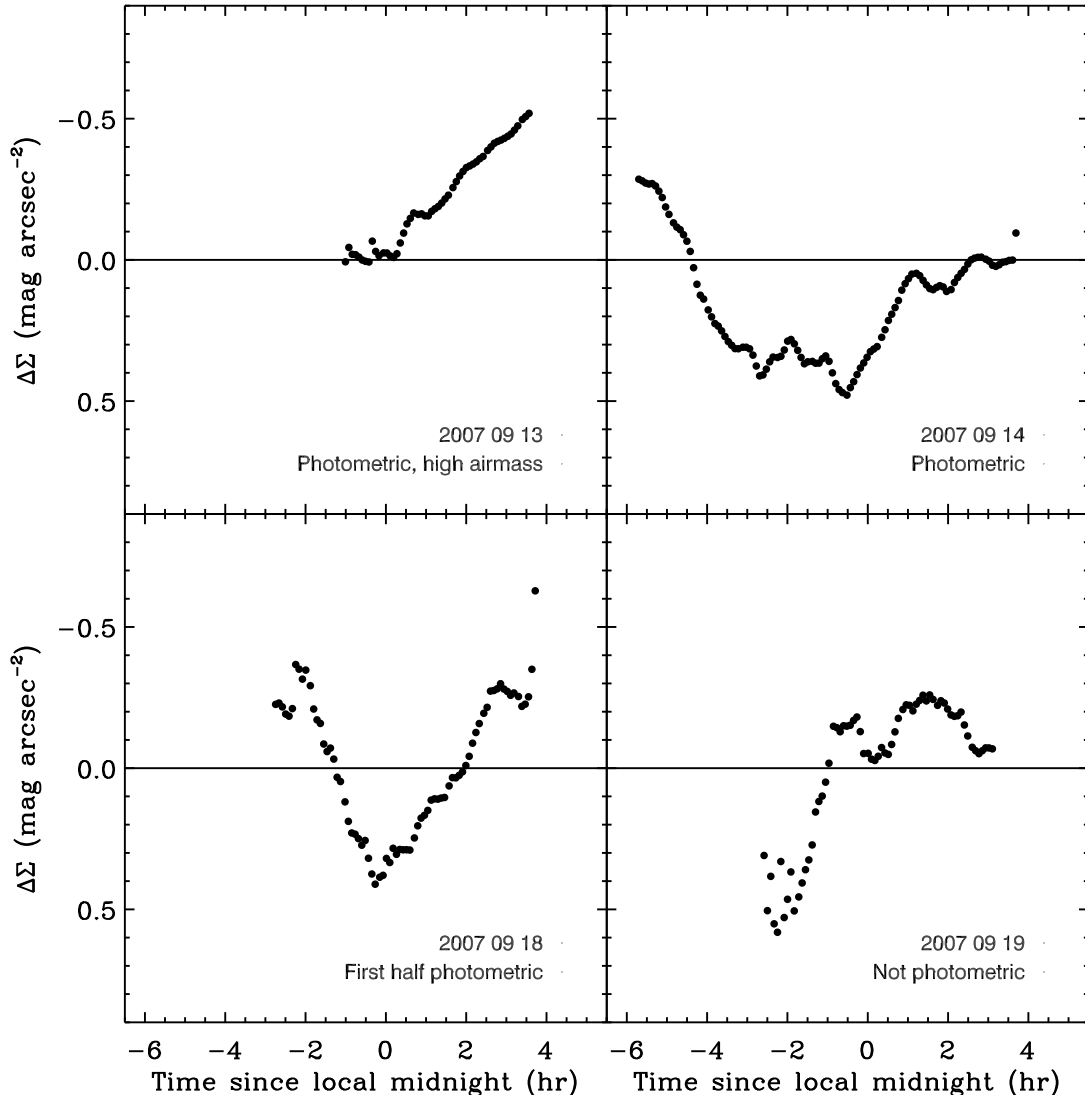


FIG. 5.— Temporal variation in y_3 band sky brightness versus time, showing highly coherent variability of up to a factor of 2 in flux over the course of a night. Flux was taken along a fixed line of sight that is 20° from the zenith and directed north. Data from the 13 and 14 are most probably photometric, the first half of the 18 may be useful, and the 19 is not photometric. The sky brightness levels in this plot were obtained from the same 2.13° radius circular region on the detector, and constitutes a differential measurement with very high signal to noise ratio. The fluctuations on both long and short timescales are real. We consider the Vega-based y_3 band zeropoint to be reliable to 0.2 mag, but this systematic uncertainty is swamped by the temporal variability in sky brightness. To convert to AB mag arcsec $^{-2}$, add 0.5 mag to the y_2^{Vega} values.

images viewed in succession is a significant overall sky level variability. The peak-to-peak variation on the 13th is 1.8 in flux, and on the 14th, 18th, and 19th are 2.0, 2.7, and 2.2 in flux, respectively. We have used a huge region of about 400 deg^2 , and we expect our statistical uncertainties from both the gravity waves and from electron counting to be subdominant to the temporal variability we measure. Changes in overall sky level are highly correlated in time, and all of the structure seen in Figure 5 is due to the atmospheric emission variability.

The relative results have made use of only ADU counts, assuming constancy for all other quantities that are needed for an absolute flux calibration. Our final task is to estimate the overall zeropoint.

6.3. Absolute Sky Brightness

In order to convert measurements from $\text{ADU s}^{-1} \text{ pixel}^{-1}$ to mag arcsec^{-2} we determined the gain, pixel scale, and magnitude zeropoint. We measured the gain to be $3.8 e^- \text{ ADU}^{-1}$. The pixel scale and zeropoint measurements were both accomplished using a standard star.

We used photometry of a type A0V standard star to establish a conversion between our instrumental magnitudes and a Vega-based y_3 band magnitude scale. This follows the approach used in Hillenbrand et al. (2002) and Hewett et al. (2006), where A0V stars are used as proxies for Vega to establish a zeropoint on the Vega magnitude scale.

We were fortunate to have beta-test access to the

TABLE 2
 ρ CETI DATA FROM THE LITERATURE.

| Band ^a | m^{Vega} | σ_m |
|-------------------|-------------------|------------|
| <i>U</i> | 4.85 | 0.03 |
| <i>B</i> | 4.85 | 0.03 |
| <i>V</i> | 4.88 | 0.03 |
| <i>J</i> | 5.08 | 0.20 |
| <i>H</i> | 4.86 | 0.02 |
| <i>K</i> | 4.81 | 0.02 |

^a *UBV* data are from Mermilliod (1987a) and *JHK* data are from Skrutskie et al. (2006).

TABLE 3
 ρ CETI DATA.

| Frame | UT | x^a (pixel) | y^a (pixel) | ϕ^b (ADU) | c^c (ADU pixel ⁻¹) |
|-------|---|------------------|------------------|-------------------|-------------------------------------|
| 110 | 06 ^h 19 ^m 01 ^s | 925.4 | 257.7 | 92.6 | 14.6 |
| 111 | 06 ^h 19 ^m 22 ^s | 923.5 | 257.8 | 117.0 | 15.5 |
| 112 | 06 ^h 19 ^m 44 ^s | 921.7 | 257.9 | 129.6 | 13.6 |
| 113 | 06 ^h 20 ^m 05 ^s | 919.1 | 257.8 | 119.2 | 15.3 |
| 114 | 06 ^h 20 ^m 26 ^s | 916.8 | 258.0 | 136.7 | 15.3 |

^a Centroid of the star.

^b ρ Ceti flux.

^c Local sky.

astrometry.net web utility (<http://astrometry.net/>), which has the remarkable ability to determine a WCS solution for an arbitrary image. We input one of our images, frame 110 (taken at UT 06^h19^m22^s) to this site and learned that the image was centered at R.A. = 01^h17^m34.8^s, Decl. = -12°20'49" (J2000). We then queried the SIMBAD archive to find A0 stars that coincided with this field. The A0V star ρ Ceti at R.A. = 02^h25^m57.0^s, Decl. = -12°17'26" (J2000) (also designated as HR 708 and SAO 148385) met our criteria. This object has cataloged magnitudes that are listed in Table 2.

We identified ρ Ceti in five of the short exposure images, and used IRAF to perform aperture photometry. The resulting centroid positions, object fluxes, and sky background values are given in Table 3. We determined the flux from the star by averaging these measurements, obtaining 119 ± 17 ADU accumulated in 20 s, or 5.95 ± 0.85 ADU s⁻¹ for an object with a Vega-based magnitude of $y^{\text{Vega}} = 4.86$ mag. This fractional flux uncertainty corresponds to a systematic uncertainty in the Vega-based magnitude zeropoint of 0.15 mag. Using the long exposures would not gain much in signal to noise ratio, because the SNR is independent of exposure time when an object trails in an image.

The rate of motion of a star at a known right ascension and declination allows for the mapping from pixels to arcseconds in the region near the star. The data from Table 3 were also used to this end. ρ Ceti was at a declination of -12.29°, implying an apparent motion across the sky of $\mu = 15'' \text{ s}^{-1} \cos 12.29 = 14.66'' \text{ s}^{-1}$. We detected the object as moving 8.6 pixel in 85 s, or 0.101 pixel s⁻¹. This implies a plate scale of 144.9'' pixel⁻¹, so that each pixel subtends an area of 20,995 arcsec², or 5.8 arcmin².

TABLE 4
 SYSTEMATIC ERROR BUDGET.

| Source | Error ^a (mag) |
|------------------------------|--------------------------|
| Sky area pixel ⁻¹ | 0.05 |
| Vega-system zeropoint | 0.15 |
| AB system zeropoint | 0.05 |
| Stray & scattered light | Unknown |
| Photometric conditions | 0.01 |
| Passband errors | Unknown |

^a Estimated upper limit of systematic error.

We consider this plate scale to be determined with a fractional uncertainty of about 5%, due to both the 1 s granularity in the timing between exposures and the centroid measurement uncertainty for the star. Our dynamic plate scale determination is also within 6% of the 153.4'' pixel⁻¹ that was returned by astrometry.net, based on matching sources across the field to cataloged objects. In one of our longer exposures we measured the trail length of a star at this same location on the array as spanning 31.2 pixels in a 300 s exposure, again confirming the plate scale determination at the 5% level.

The calibration source, and the region around it where we determined the sky brightness values, reside near a corner of the field. The rays that are brought to a focus at this location pass through the filter at an angle of 18.6°, while the median LSST incidence angle is 18.9°. We therefore consider the center of our effective passband at this location to be a good match to LSST's, but the shape at the passband edges will still differ somewhat.

With the photometric calibration and plate scale in hand, we were in a position to convert the sky brightness values, Σ , into Vega-based units of mag arcsec⁻². We converted the sky brightness values into units of ADU s⁻¹ arcsec⁻² by dividing by 20,995 arcsec² pixel⁻¹. We then computed the Vega-based sky brightness using the flux from the comparison star, as

$$\Sigma^{\text{Vega}} = -2.5 \log(\phi/5.95) + 4.85 \frac{\text{mag}}{\text{arcsec}^2} \quad (2)$$

where ϕ is the sky flux in ADU s⁻¹ arcsec⁻². Note that we selected a region for sky brightness determination that surrounded the calibration star to minimize our sensitivity to large scale flatfielding errors and pixel scale variations. The final zeropoint that converts all temporal results of Figure 5 to Vega magnitudes is $\Sigma = \Delta\Sigma + 17.8$ mag arcsec⁻² (Vega).

We also supply the conversion of Vega magnitudes through the *y* band to AB magnitudes, because, while the AB and Vega magnitude scales are matched at the V band, they monotonically diverge at longer wavelengths. The Spitzer flux conversion utility¹ delivers $AB_y^{\text{Vega}} = 0.5$ mag with an uncertainty of 0.05 mag., where $y^{\text{AB}} = y^{\text{Vega}} + AB_y^{\text{Vega}}$. This level of uncertainty is adequate for our purposes here. The conversion also agrees within the uncertainties with the AB-to-Vega offset terms presented in Table 7 of Hewett et al. (2006). Thus the conversion $\Sigma = \Delta\Sigma + 18.3$ mag (AB) brings all temporal results of Figure 5 into the AB system. Table 4 presents a summary of the potential sources of system-

¹ At <http://ssc.spitzer.caltech.edu/warmmission/propkit/pet/magtojy/>

atic error that might afflict these results.

7. CONCLUSIONS

We have performed first measurements of y_3 band sky brightness in Chile from Cerro Tololo, and have argued that these results to apply to the nearby LSST site on Cerro Pachon. We observed rms spatial variability of 3–4% due to atmospheric gravity waves on scales of a few degrees and larger, and a factor of 2 variability in flux over the course of the nights we observed. These relative results make no reference to absolute calibrations, and we argue that they apply to nearly any y band variant because the sky background is overwhelmingly due to narrowband OH emission. Finally, we estimate an absolute zeropoint and find the mean sky level is about 17.8 mag arcsec⁻². Our absolute calibration suffers up to 20% systematic uncertainty from zeropoint and pixel scale measurement errors, while our relative photometry is uncertain at about a percent.

Previous aeronomy work has characterized the OH background in depth, and suggests that the variability is somewhat predictable. We expect the sky background through any similar, CCD-based y band variant to fluctuate significantly, although nominal variation and absolute levels will differ depending on the precise nature of the total filter response curve. Our qualitative results and conclusions should apply to any y band.

The variability suggests that sky survey projects would benefit from a y band sky brightness monitor, and an adaptive strategy that would exploit times when the y sky is dark to take observations in this band. The background in y appears uniform to within 4% over much of the sky, so we advise it is better to chase *times* of low background than to find *directions* of dark sky in y . The coherent spatial structures in y band airglow present a

potential difficulty to sky-based illumination correction strategies. Assuming random Gaussian fluctuations, 15 images or more are needed to achieve sub-percent uniformity over fields of view larger than about a degree. The spatial coherence of the gravity waves means the fluctuations are not random, making this a lower limit.

We have demonstrated the effectiveness of this apparatus. Given the observed variability in y_3 band sky brightness, there is considerable merit in implementing a long term monitor at the LSST site. Having long term sky brightness data in hand early will inform the optimal scheduling of the LSST system.

We thank the LSST Corporation, Harvard University and the Department of Energy Office of Science and the National Science Foundation for their support. The LSST design and development activity is supported by the National Science Foundation under Scientific Program Order No. 9 (AST-0551161) through Cooperative Agreement AST-0132798. Additional funding comes from private donations, in-kind support at Department of Energy laboratories and other LSSTC Institutional Members. We thank the CTIO scientific and technical staff for their invaluable help in setting up these observations. We are also very grateful to the team that is establishing the *astrometry.net* (<http://astrometry.net/>) online resource, which we used in its testing phase to determine the centers of the images we obtained. The authors gratefully acknowledge the referee for insightful comments and recommendations. This publication makes use of data products from the Two Micron All Sky Survey, which is a joint project of the University of Massachusetts and the Infrared Processing and Analysis Center/California Institute of Technology, funded by the National Aeronautics and Space Administration and the National Science Foundation.

REFERENCES

- Baker, D. J., & Stair, A. T., Jr. 1988, *Phys. Scr.*, 37, 611
 Cosby, P. C., Sharpee, B. D., Slanger, T. G., Huestis, D. L., & Hanuschik, R. W. 2006, *Journal of Geophysical Research (Space Physics)*, 111, 12307
 Cosby, P. C., & Slanger, T. G. 2007, *Canadian Journal of Physics*, 85, 77
 Garcia, F. J., Taylor, M. J., & Kelley, M. C. 1997, *Appl. Opt.*, 36, 7374
 Hewett, P.C. et al. 2006, *MNRAS*, 367, 454.
 Hillenbrand, L. et al. 2002, *PASP*, 114, 708.
 Kaiser, Nicholas et al. 2002, *Proc. of the SPIE*, 4836, 154
 Krisciunas, K. et al. 2007, *PASP*, 119, 687
 Li, F., Liu, A. Z., Swenson, G. R., Hecht, J. H., & Robinson, W. A. 2005, *Journal of Geophysical Research (Atmospheres)*, 110, 9
 LSST Science Collaborations: Paul A. Abell, et al. 2009, arXiv:0912.0201
 Marsh, D. R., Smith, A. K., Mlynczak, M. G., & Russell IIIJ. M., 2006, *J. Geophys. Res.*, 111, A10S05
 Meinel, I. A. B. 1950, *ApJ*, 111, 555
 Meinel, A. B., II 1950, *ApJ*, 112, 120
 Melo, S. M. L., Lowe, R. P., & Russell, J. P. 2000, *J. Geophys. Res.*, 105, 12397
 Mermilliod, J.-C., 1987 *Astron. Astrophys. Suppl. Ser.* 71, 413
 Nakamura, T., Higashikawa, A., Tsuda, T., & Matsushita, Y. 1999, *Earth, Planets, and Space*, 51, 897
 O'Connor, P. et al. 2006, *Proc. of the SPIE*, 6276, 53.
 Patat, F. 2003, *A&A*, 400 1183
 Puxley, P. and the Gemini Observatory 2001, <http://www.gemini.edu/sciops/ObsProcess/obsConstraints/atm-models/sk>
 Rousselot, P., Lidman, C., Cuby, J.-G., Moreels, G., & Monnet, G. 2000, *A&A*, 354, 1134
 Sanchez, F. et al. 2007, *PASP*, 119, 1186.
 Skrutskie, R.M. et al. 2006, *AJ*, 131, 1163
 Taylor, M. J., & Hill, M. J. 1991, *Geophys. Res. Lett.*, 18, 1333
 Warren, S. J., et al. 2007, *MNRAS*, 375, 213
 Wiens, R. H., et al. 1997, *Advances in Space Research*, 19, 677